

TECHNISCHE UNIVERSITÄT DORTMUND

PHYSICS DEPARTMENT

INTERNATIONAL MASTER ADVANCED METHODS IN PARTICLE PHYSICS

Characterization of Silicon Strips Detectors

Laboratory report

Date: July 21, 2024

Simone Garnero - simone.garnero@tu-dortmund.de

Bastian Schuchardt - bastian.schuchardt@tu-dortmund.de

Contents

1	Introduction	2
2	Theory	3
2.1	Semiconductors	3
2.2	P-N junction	4
3	Experiment	5
3.1	Detector unit	6
3.2	Control unit	6
3.3	Pedestal and noise	6
4	Analysis	7
4.1	Pedestal run	7
4.2	Calibration measurements	8
4.3	Measuring the strip sensor by using the laser	10
4.4	Charge collection efficiency	12
4.4.1	Laser	13
4.4.2	Beta source	14
4.5	Large Source Scan	15
4.6	Discussion	16

Analysis of Silicon Strips sensors for the ATLAS experiment

Advanced Laboratory Course: Particle Physics

Simone Garnero, Bastian Schuchardt

July 21, 2024

Abstract

The goal of this laboratory experience is to determine the properties of silicon strip detectors, understand their functioning, and explain why they are used as tracking devices in particle physics experiments like ATLAS. This has been achieved by a series of tests carried out with a laser and a β^- -radiation source, after a calibration and noise reduction process.

1 Introduction

In many experiments, the area closest to the interaction point is covered by silicon detectors. In ATLAS, for example, one of the four major experiments at LHC built cylindrically around the beam pipe, the first subdetector encountered is the *Inner Detector* (ID), composed of three elements: the *Pixel Detector*, the *Silicon Strip Detector*, and the *Transition Radiation Tracker* (TRT). Among these, pixel sensors are the most highly structured and thus have better spatial resolution. However, they are more expensive. Therefore, since the further from the beam pipe, the larger the area to cover, they are only used as the innermost layer. The second component of the ID is the silicon strip detector, which consists of four double layers of silicon strip sensors. To improve the resolution, they are twisted by 40 mrad. In the ATLAS experiment, this silicon strip detector comprises 4088 individual modules, each containing 768 strips. For this experiment, the focus is on this specific type of sensor. The sensors utilized in the laboratory are, naturally, a simplified version of those described for the ATLAS experiment. Specifically, they contain only 128 individual strips. The analysis presented in this report aims to deduce the properties of this type of sensor using two different radiation sources. In fact, after the measurement of a current-voltage characteristic, an evaluation and reduction of noise and background, some calibration measurements have been carried out using a laser source, in order to observe how the sensor responds to a controlled source. Subsequently, the laser was replaced with a radioactive source to create a more realistic situation. The isotope used was ^{90}Sr , which undergoes β -decay, producing ^{90}Y , which in turn decays again, emitting more electrons and producing ^{90}Zr .

2 Theory

2.1 Semiconductors

Semiconductors are very important for today's electronics because of their electrical properties. These properties are characterized by the size of the band gap, which is defined as the energy gap between the conduction and the valence band [1]. Insulators have large band gaps, usually greater than 4 eV, whereas in conductors the gap is non-existent, with the conduction and valence bands overlapping. Semiconductors are in between, with a very small band gap, so that electrons can reach the conduction band with a small excitation. Silicon, for example, is one of the most common semiconductors in electronics, along with germanium, and has a band gap of 1.107 eV. Its atoms arrange themselves to create a crystalline structure. When an electron is excited, it leaves the covalent bonds in the structure and gets to the conduction band. Doing so, it leaves a positively charged atom and a "hole", which can be considered as a quasiparticle, and can generate a positive current. Normally after the excitation, recombination occurs; but if there is an electric field, electrons move to the anode and holes to the cathode. The conductivity of an element depends on its charge carrier density. In order to increase it, one can resort to a process called *doping* [2], which consists of inserting impurities in the original semiconductors. Those impurities are atoms of another element with a different number of valence electrons. There are two types of doping:

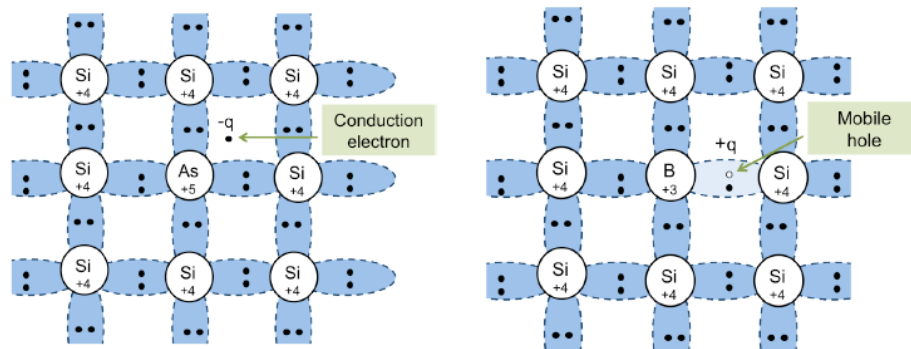


Figure 1: Schematic representation of n-type doping using Arsenic and p-type doping with Boron, respectively. The crystalline structure is visible, and the charge carriers are highlighted. [3]

- **n-type:** Atoms with a greater number of valence electrons are added to the original lattice. In this way, one electron is unnecessary for the bond and is free to move in the lattice. The doping atom is referred to as a *donor*. In Figure 1 (left), silicon doping with Arsenic has been chosen as an example.
- **p-type:** In this case, atoms with a smaller number of valence electrons are chosen to be added to the semiconductor structure. In Figure 1 (right), Boron only has three valence electrons that are involved in the bond. The total structure is neutral, but there is a "hole" in one of the covalent bonds, which can be filled by another electron. That's why, in this case, the doping atom is called an *acceptor*.

2.2 P-N junction

When, in the same semiconductor, an n-type region and a p-type region come into contact, a p-n junction is formed [4]. Initially, since one part has an abundance of electrons and the other side has many holes, charge carrier diffusion between the two layers is activated. As soon as the charge carriers go through the junction, recombination processes begin. This implies that positively and negatively charged ions remain in the n-region and p-region, respectively, creating an electric field that stops the migration of the charges. Thus, in a small fraction of time, an equilibrium situation is reached. In these conditions, the region over the junction is filled by fully recombined ions and is called *depletion region*. In Figure 2, a schematic p-n junction is depicted. If a potential difference is applied across the terminals of the p-n junction, it is called a diode. Depending on where one connects the anode, one can have a diode in forward bias or in reverse bias and they have completely different properties.

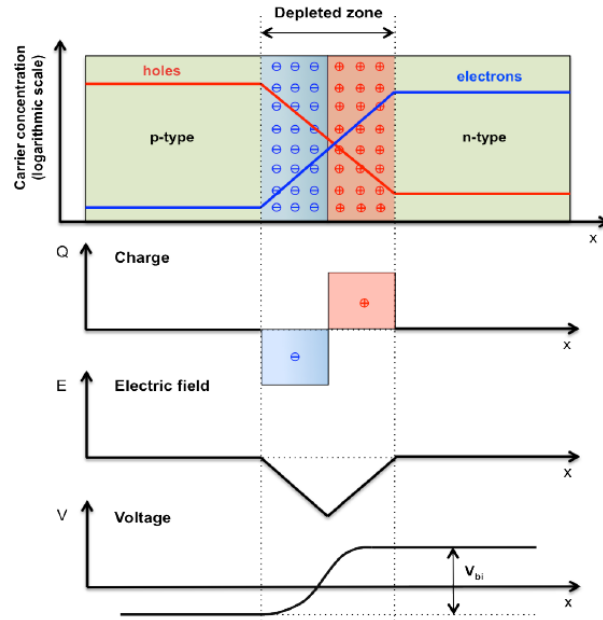


Figure 2: Schematic picture of a p-n junction. Underneath the junction, plots showing the charge, the electric field, and the voltage as a function of distance are depicted. [3]

The one of interest here for particle detection is the reverse bias because recombination is undesirable. So, the anode is connected to the n-side and the cathode to the p-side, and the immediate consequence is an expansion of the depletion region. Its thickness depends on the applied bias voltage U as

$$d(U) = \sqrt{\frac{2\epsilon(U_D + U)}{qN_{eff}}}, \quad (1)$$

with ϵ being the dielectric constant of silicon, U_D the diffusion voltage at equilibrium, q the elementary charge and N_{eff} the effective charge carrier density, defined by the concentrations

of donor (N_D) and acceptor (N_A) atoms in the junction:

$$N_{\text{eff}} = \frac{N_D N_A}{N_D + N_A}. \quad (2)$$

Since this experiment uses the diode as a detector, recombination must be avoided to allow observation of the particles. Therefore, the depletion region should spread over the entire crystal. Considering $U \gg U_D$ and rearranging Equation 1, the voltage at which the junction is fully depleted is:

$$U_{\text{dep}} \approx \frac{q}{2\epsilon} N_{\text{eff}} D^2 \quad (3)$$

In this condition, there should be no current flowing through the semiconductor. However, thermal excitation leads to the creation of electron-hole pairs which are then separated by the electric field and generate a small current, referred to as *leakage current*.

3 Experiment

For the experiment, the Educational Alibava System (EASy) [3] has been used. It is a system developed especially for students by the company Alibava Systems. It includes the experimental apparatus and software for the data acquisition. The system consists of three components: the control unit, the detector unit, and a computer that performs the data acquisition. A graphical user interface (GUI) allows the user to access the control unit.

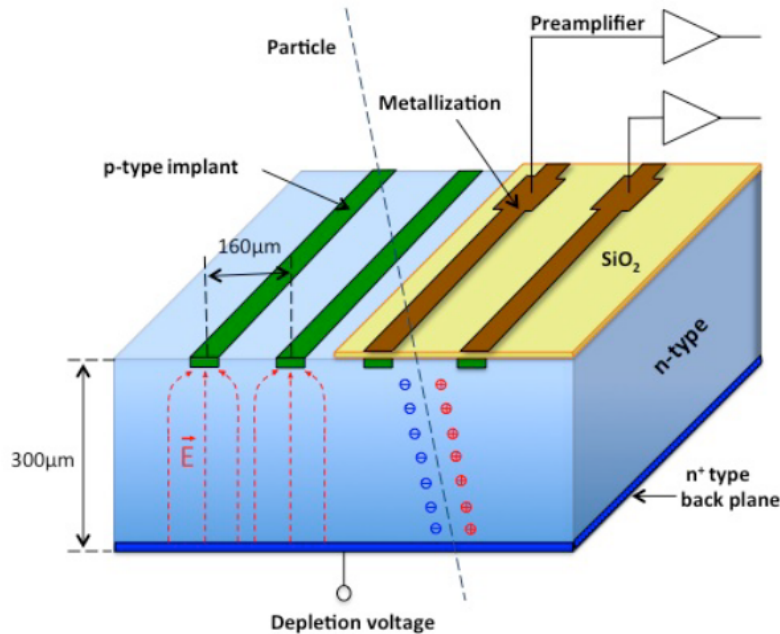


Figure 3: Sketch of the EASy silicon sensor. An ionizing particle going through the diode is depicted, showing the electrons that are then pushed by the electric field to the n-doped strips, where the signal is detected. [3]

3.1 Detector unit

The detector unit includes the semiconductor sensor and the read-out electronics. The detector is a p-in-n sensor. This is because it consists of a 300 μm thick n-doped silicon layer, in which 128 p-doped silicon strips are embedded, spaced 160 μm apart. In Figure 3, a schematic picture of the sensor is shown. As explained in Subsection 2.2, the semiconductor must be fully depleted to perform properly. If this is not the case, the electron-hole pairs recombine outside the depletion region, making them undetectable. Indeed, the charge collection efficiency (CCE) reaches its maximum at U_{dep} and decreases with lower potential. In the case of the laser, it depends on the potential in the following manner:

$$CCE(U) = \frac{1 - \exp\left(\frac{-d_c(U)}{a}\right)}{1 - \exp\left(\frac{-D}{a}\right)} \quad (4)$$

with d_c the thickness of the depletion region, D the sensor thickness and a the mean penetration depth of laser into silicon. Underneath the sensor, there is an additional silicon diode that detects the electrons that have passed through the entire sensor and emits a trigger signal. The read-out chip used in this experiment is the BEETLE, which is also used in the LHCb experiment. It amplifies incoming charge signals and converts them into voltage signals, which are then converted into ADC counts in the control unit. On top of the detector unit, there is a sliding platform containing a laser system and a carbon plate for the source measurement. The laser has a wavelength of 980 nm, a peak power of 0.6 mW, and a pulse length of 5 ns. The focus and position of the laser can be adjusted by two-micrometre screws.

3.2 Control unit

The control unit is used to control the detector unit. From here one can modify the bias voltage of the diode. To interact with this unit, a graphical user interface is provided. With that, one can start the data recording, select the operating mode, display the data, and save them.

3.3 Pedestal and noise

As is the case with every sensor, the silicon strip detector also generates noise. The goal is to evaluate it and reduce it to the minimum. To achieve this, the measured $ADC(i, k)$ count for a signal k at a strip i is analyzed as follows:

$$ADC(i, k) = P(i, k) + D(k) + Signal(i, k) \quad (5)$$

where $P(i, k)$ is the *pedestal*, i.e. the mean value of ADC counts for a strip when no external signal is applied, and is computed from N measurements as:

$$P(i) = \frac{1}{N} \sum_{k=1}^N ADC(i, k), \quad (6)$$

and D_k is the *common mode shift*, a global disturbance affecting all strips during an event, which is determined by:

$$D(k) = \frac{1}{128} \sum_{i=1}^{128} (ADC(i, k) - P(i)). \quad (7)$$

For each strip, the noise is determined by subtracting the pedestal and common mode shift from the ADC counts and taking the standard deviation:

$$Noise(i) = \sqrt{\frac{1}{N-1} \sum_{k=1}^N (ADC(i, k) - P(i) - D(k))^2} \quad (8)$$

4 Analysis

The depletion voltage of the sensor was determined by measuring the current-voltage characteristic. The leakage current according to a bias voltage can be seen in Figure 4. The curve flattens after the point at 80 V, which agrees with the depletion voltage given by the manufacturer. To ensure that the chip is always fully depleted for the following measurements a bias voltage of 80 V has been set.

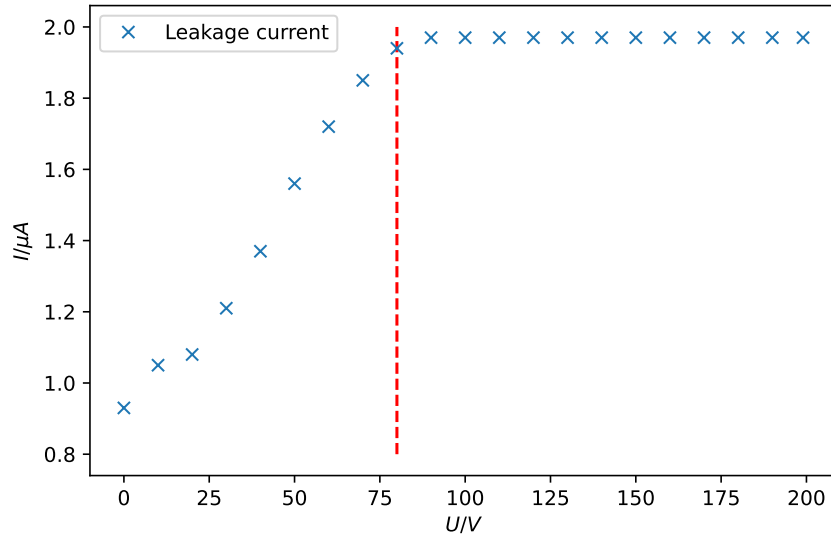


Figure 4: Leakage current in μ A for a bias voltage in V.

4.1 Pedestal run

To determine the noise, the pedestal runs are used and the mean values of the ADC counts for each strip are computed, according to Equation 6. Then, the noise can be obtained from Equation 8 by plugging in the common mode shift from Equation 7. Bar plots of the pedestal run and noise can be seen in Figure 5.

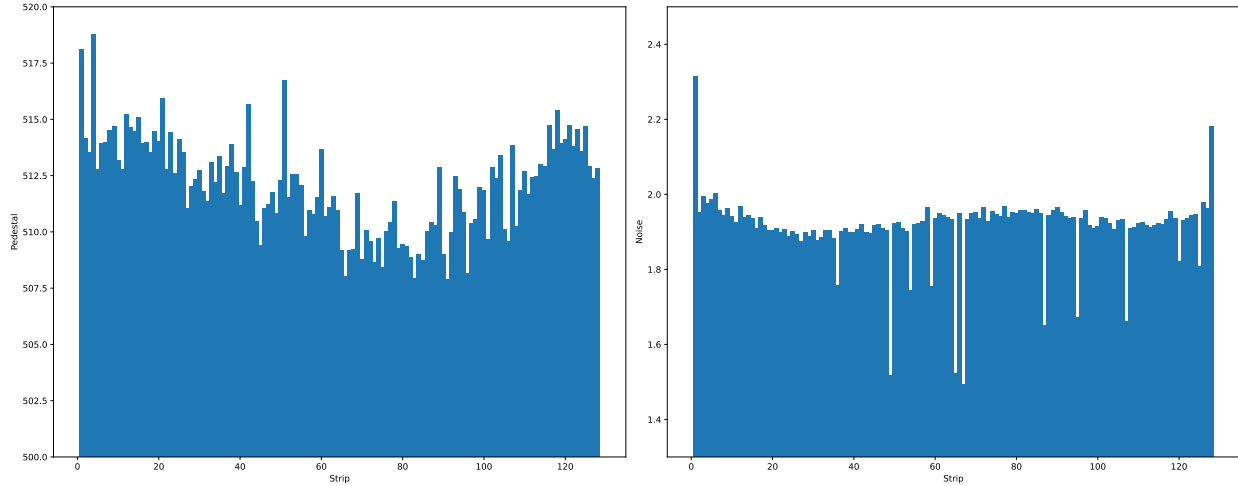


Figure 5: Bar plots of the pedestal run (left) and noise (right).

For the pedestal and noise run, large increases towards the edges of the strips can be seen. The histogram of the common mode shift can be seen in Figure 6. The histogram has been normalized and shows the expected shape of a Gaussian distribution with a mean around zero.

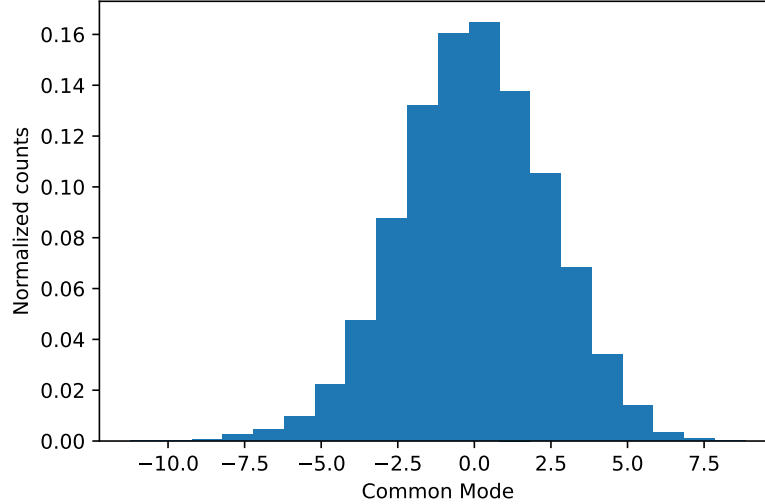


Figure 6: Common mode shift of the pedestal run.

4.2 Calibration measurements

After determining the best delay value, a delay of 64 ns has been chosen for the calibration measurement. Four different calibration measurements can be seen in Figure 7.

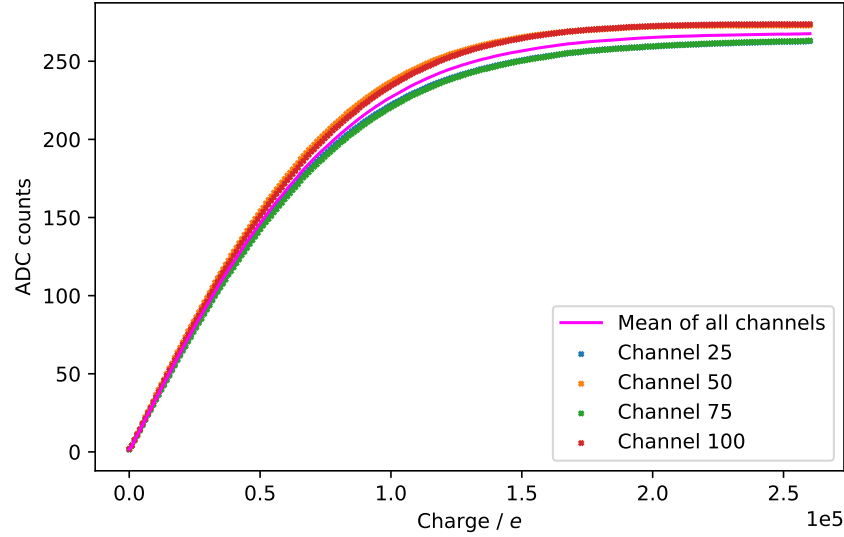


Figure 7: ADC counts plotted against the injected charge per elementary charge for four channels and the mean of all channels.

The calibration curves of channels 25 and 75 are similar. The same is true for channels 50 and 100. Why channels 25 and 75 have a lower calibration curve than channels 50 and 100 could not be determined. Moreover, channels 25 and 75 skew the mean of the four channels to lower values. Additionally, the curve of channel 50 can be compared to the same channel at 0 V in Figure 8.

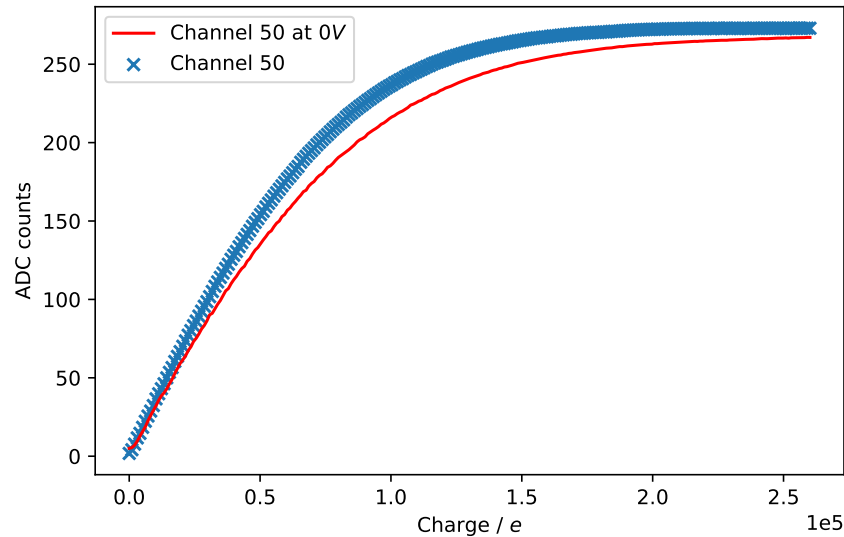


Figure 8: Caption

The channel at 0 V has slightly fewer ADC counts than the calibration curve of the channel with a bias voltage applied. The difference is especially noticeable around $1.0 \cdot 10^5 \frac{1}{e}$ and less

apparent towards the beginning and end of the curve. This behaviour is expected because a lower bias voltage results in a smaller depletion zone which subsequently leads to fewer ADC counts measured. Additionally, a fourth-degree polynomial of the form

$$Q(ADC) = a \cdot ADC^4 + b \cdot ADC^3 + c \cdot ADC^2 + d \cdot ADC + e$$

was fitted to further investigate the dependency of the ADC counts on the injected charge. Only ADC counts below 250 were considered to get better results. The fit can be seen in Figure 9.

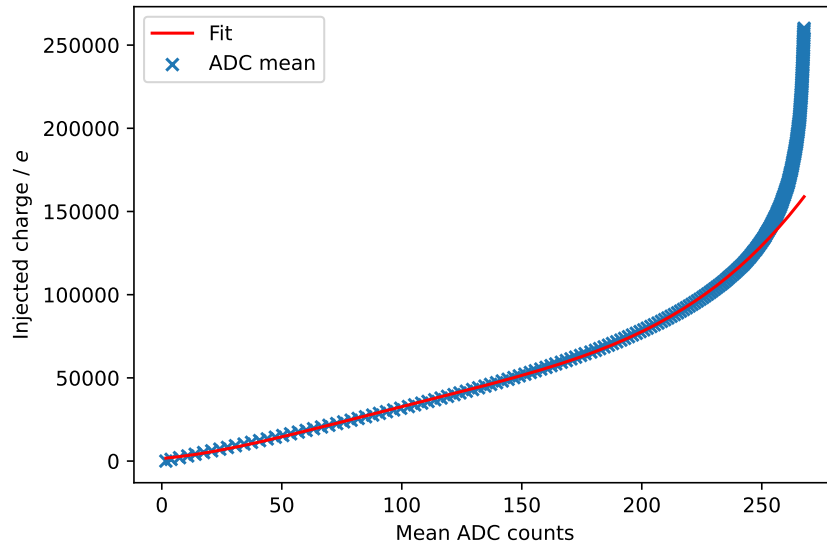


Figure 9: Caption

The fit parameters were obtained to be

$$a = (7.4 \pm 0.4) \cdot 10^{-5} e$$

$$b = (2.8 \pm 0.2) \cdot 10^{-2} e$$

$$c = (3.92 \pm 0.35) e$$

$$d = (125 \pm 23) e$$

$$e = (1.5 \pm 0.4) \cdot 10^3 e.$$

With the fit parameters and the fourth-degree polynomial fit, it is possible to convert the ADC counts to energy values in keV.

4.3 Measuring the strip sensor by using the laser

The structure of the strip sensor can be measured by using a laser. Before the measurement, the optimal delay of the laser was determined to be 100 ns. The laser sync run that yielded this result can be seen in Figure 10.

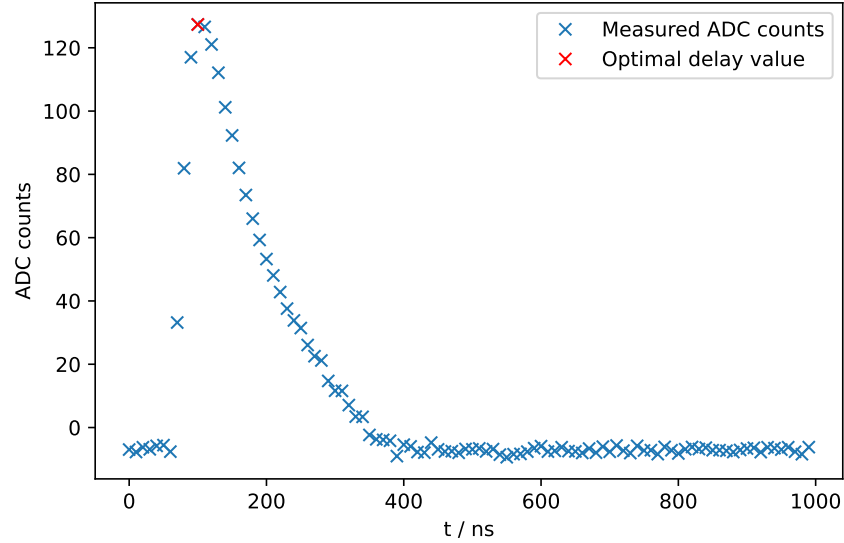


Figure 10: Measured ADC counts of the laser sync run. The optimal delay value at 100 ns is highlighted in red.

The laser was moved in $35 \mu\text{m}$ intervals and the signal in the channels of the strip sensor was measured. A heatmap of the channel signals from 99 to 105 can be seen in Figure 11.

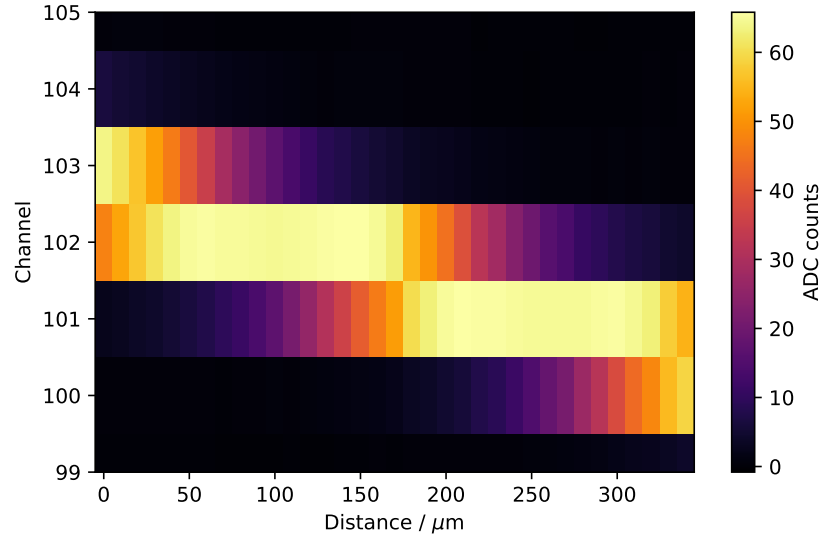


Figure 11: Heatmap of the signal strength for the position of the laser.

The heatmap does not show the expected result. There should be two peaks per channel but only one can be noticed. This behaviour can probably be explained by a bad focus of the laser which should have been checked beforehand. To further analyse the peaks, channel 102 was chosen. A plot of the signal strength can be seen in Figure 12.

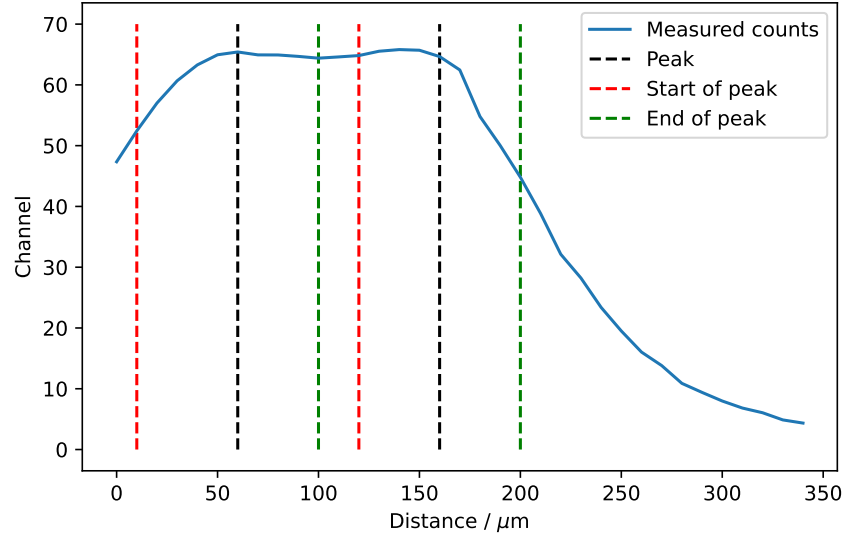


Figure 12: Signal strength of channel 102 for the laser position.

From these results, the physical structure of the strips can not be faithfully determined. But by assuming that the small dip in the middle of the large peak is the end of the two expected peaks a rough estimate of the structure of the strip can be made. The structure can be estimated to

$$\text{width of the strip} \approx 160 \mu\text{m} - 60 \mu\text{m} = 100 \mu\text{m}$$

$$\text{laser extension} \approx 160 \mu\text{m} - 120 \mu\text{m} = 40 \mu\text{m},$$

where the width of the strip was determined by the distance between the two maxima and the laser extension is the distance between the maximum of the peak and the end of the peak. Moreover, the distance between two strips can be determined from Figure 11 by comparing the position of the maxima between two channels. The pitch can then be calculated as the sum of the width of the strip and the distance between two strips to

$$\text{distance} \approx 70 \mu\text{m}$$

$$\text{pitch} \approx 100 \mu\text{m} + 70 \mu\text{m} = 170 \mu\text{m}.$$

It should be noted that these results could not have been obtained without knowing the basic structure of the strips and are just rough estimates of the true structure.

4.4 Charge collection efficiency

The charge collection efficiency can be determined by measuring the ADC counts for an applied bias voltage. For this measurement, the laser and a beta source were used.

4.4.1 Laser

To get the charge collection efficiency, the channel in which the laser is focused must be determined. For this reason, a heatmap of each channel was produced and can be seen in Figure 13. The heatmap shows clearly that the laser is focused on channel 83. For the rest of this part of the analysis, only channel 83 is considered.

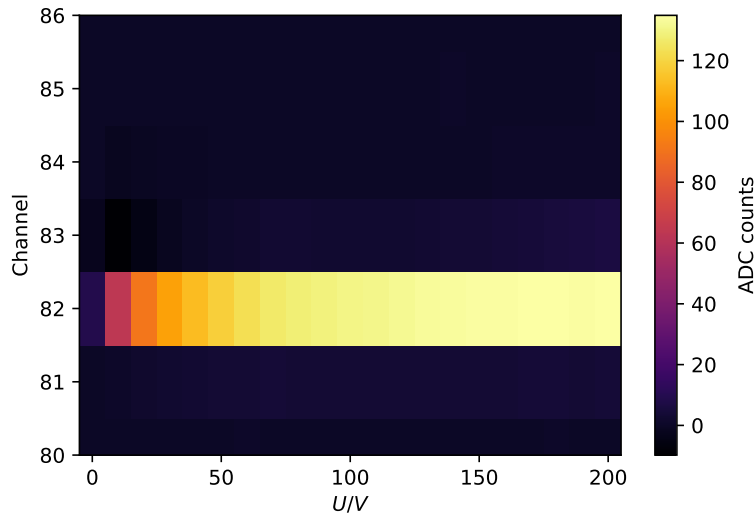


Figure 13: Heatmap of all channels.

To get the charge collection efficiency the data were shifted upwards so that all values are positive and have been normalized so that they are in a range between zero and one. The charge collection efficiency of channel 83 can be seen in Figure 14.

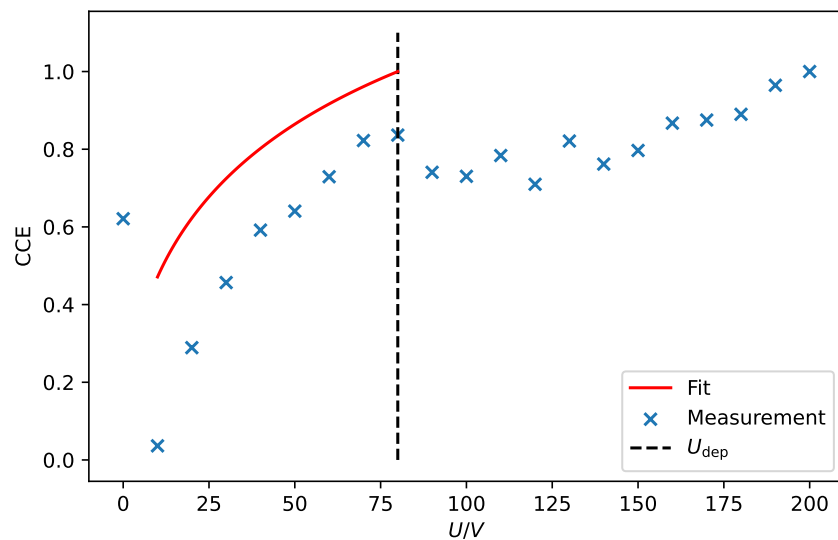


Figure 14: Charge collection efficiency of channel 83.

For an unknown reason, the first measurement is not at zero but was still considered for the fit. Furthermore, the charge collection efficiency drops after the depletion voltage and just roughly resembles the shape of a plateau. The fit was done in a range between 0 V and 80 volt which is the depletion voltage. From the fit according to Equation 4 the penetration depth of the laser was determined to

$$a = (30 \pm 40) \mu\text{m}.$$

The determined penetration depth is too low and the uncertainty too high to make any statement about the penetration depth. The measurement failed for an unknown reason that could not later be explained.

4.4.2 Beta source

The charge collection efficiency can be determined by using a radioactive β^- source. This measurement was not possible because of a damaged cable and measurements furnished by the supervisor were used. In Figure 15 the curve of the β^- source and the curve of the laser are given. The charge collection efficiency of the β^- source has been computed by summing the ADC counts of the clusters and taking the mean for each cluster. Additionally, the curve has been normalized.

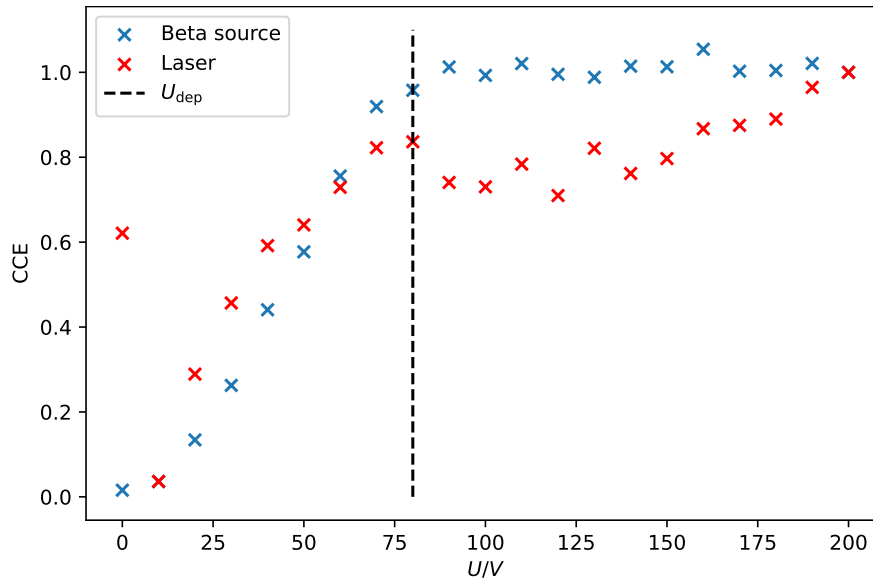


Figure 15: Curves of the charge collection efficiency determined by the laser and the β^- source.

Comparing the curves it is clear that the measurement charge collection efficiency of the laser was wrong because it is expected that both curves agree after reaching the depletion voltage of 80 V. It can be seen that the laser has a higher collection efficiency for lower bias voltages than the β^- source. This can be explained by the fact that the strip sensor performs worse for detecting charged particles at lower voltages.

4.5 Large Source Scan

For the large source scan, given by the supervisor was used. The number of clusters and the number of channels per cluster are given in Figure 16. It can be seen that one event usually leads to one cluster. It is rare that there are zero or two clusters. Furthermore, one cluster consists of up to six channels, where one or two channels is the most common number of channels.

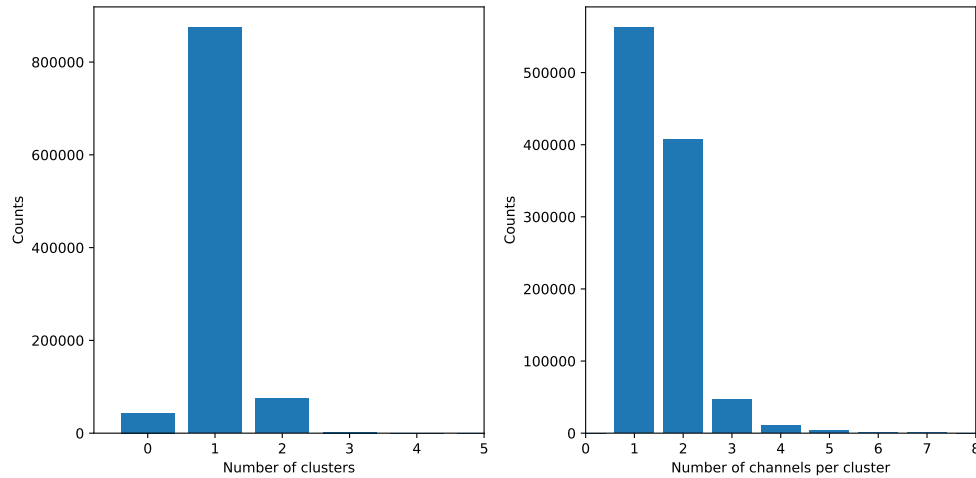


Figure 16: Number of clusters (left) and number of channels per cluster (right) for large source scan.

A hitmap of the channels is given in Figure 17. The most hits are around channel 80 and they drop off towards the edges.

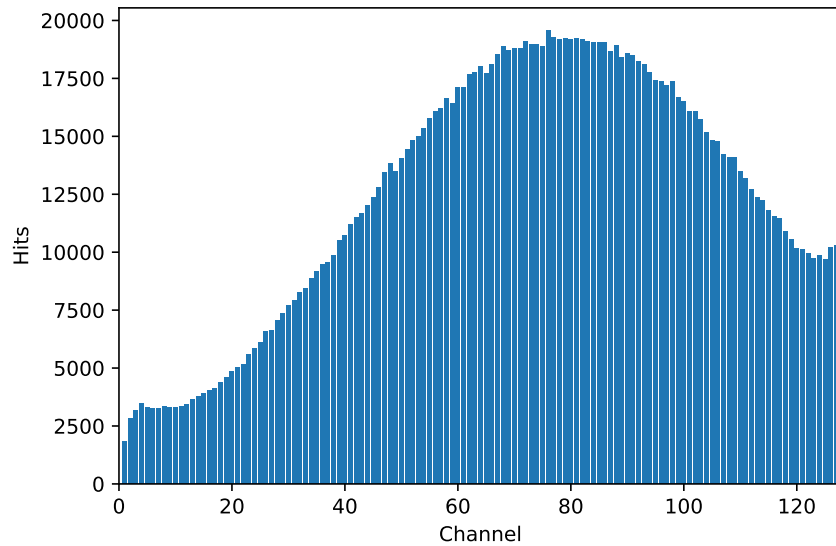


Figure 17: Hitmap of the events of each channel.

At last, the energy distribution can be obtained from the distribution of the ADC counts. Both distributions are given in Figure 18. The ADC count distribution was converted to an energy distribution by using the fit parameters obtained from the calibration measurement and the fact that the energy needed for the generation of an electron-hole pair is 3.6 eV.

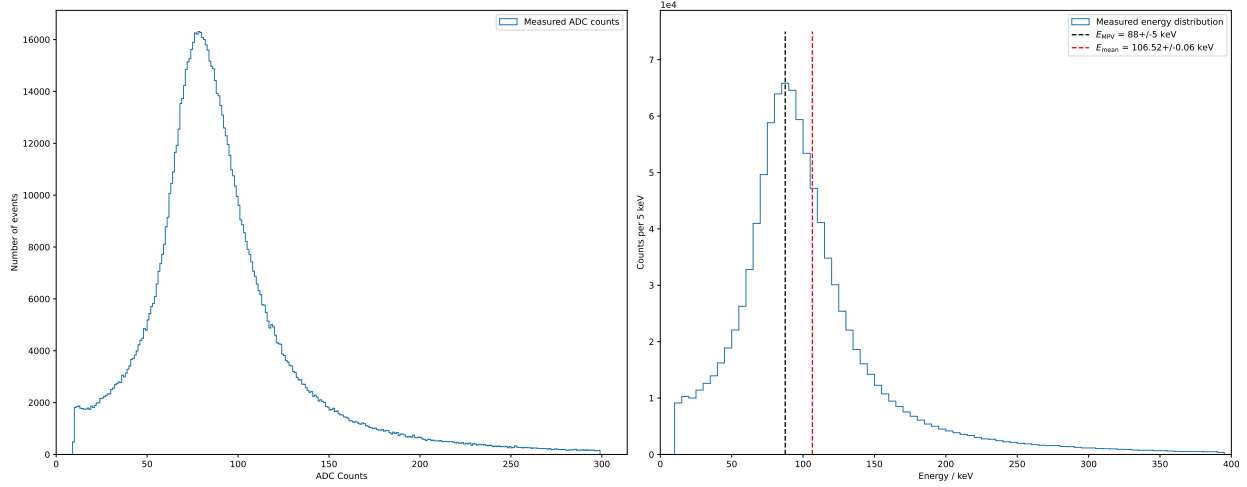


Figure 18: Distribution of ADC counts (left) and energy distribution (right).

The most probable value and the mean value of the energy distribution were determined to

$$E_{MPV} = (88 \pm 5) \text{ keV}$$

$$E_{mean} = (106.52 \pm 0.06) \text{ keV}.$$

4.6 Discussion

According to the manufacturer, the depletion voltage lies between 60 V and 80 V. From the leakage current a depletion voltage of 60 V was determined. The charge collection efficiency curves yield a depletion voltage of 80 V. Both values lie in the range given by the manufacturer. The pedestal run, the noise run, and the common mode shift showed the expected behaviour. The calibration measurement mostly agrees with the expectations but two of the channels have a lower curve than the other two which skews the mean curve to lower values. Nevertheless, the fit of the mean ADC counts yielded parameters that later were able to arrive at an energy distribution that agrees with theory values. In contrast to the other measurements, the measurements using the laser were unsuccessful likely because the laser was not focused properly. The heatmap of the signal strength shows one large peak and not two peaks like expected. With the knowledge of the structure of the chip, rough estimates could be deduced. The width of the strip is 100 μm , the laser extension is 40 μm , the distance between two strips is 70 μm , and the pitch is 170 μm . The charge collection efficiency for the laser was shifted upwards so no negative values were there and normalized. This is another sign for a bad measurement because only the normalization of the data would be needed if everything went right. Additionally, the first measurement was not at zero. Subsequently, a penetration depth of the laser of $(30 \pm 40) \mu\text{m}$ was derived from the

fit which can not be right. The comparison of the charge collection efficiency of the laser with the charge collection efficiency of the beta source showed a better performance of the laser for lower bias voltages as expected. The laser and β^- curves do not match after the depletion voltage of 80 V which is another sign of a bad measurement. It must be noted that all measurements involving a radioactive source were not carried out by us because of a damaged cable. Finally, the energy spectrum of the large source scan agrees with the theoretical expectation of a convoluted Gauss and Landau curve, where the most probable value is smaller than the mean value of the distribution. The mean value of the distribution was obtained to be $E_{mean,exp} = (106.52 \pm 0.06) \text{ keV}$. A deviation of 27.9% with respect to the theory value of $E_{mean,exp} = (146.5 \pm 0.6) \text{ keV}$, which is acceptable considering the fact that different data were used for the analysis.

In conclusion, it can be said that all but the measurements using the laser were successful and agreed with their expectations. Probably the laser was not focused properly, but other explanations can not be ruled out confidently.

References

- [1] Helmuth Spieler. *Semiconductor detector systems*, volume 12. Oxford university press, 2005.
- [2] E Fred Schubert. *Delta-doping of semiconductors*. 1996.
- [3] Alibavasystems. *Activity Book for Students*. 2015. First edition. Barcelona.
- [4] J. Millman and A. Grabel. *Microelectronics*. Electrical & electronic engineering series. McGraw-Hill, 1987.